International Journal of Heat and Mass Transfer 198 (2022) 123399

Contents lists available at ScienceDirect

International Journal of Heat and Mass Transfer

journal homepage: www.elsevier.com/locate/hmt

Dropwise condensation reduces selectivity of sky-facing radiative cooling surfaces

Eylul Simsek[a], Jyotirmoy Mandal[b], Aaswath P. Raman[b,c], Laurent Pilon[a,c,d,*]

[a] Mechanical and Aerospace Engineering Department, University of California, Los Angeles, Los Angeles CA 90095-1597, USA
[b] Department of Materials Science and Engineering, University of California, Los Angeles, Los Angeles CA 90095-1595, USA
[c] California NanoSystems Institute, University of California, Los Angeles, Los Angeles, California 90095, USA
[d] Institute of the Environment and Sustainability, University of California, Los Angeles, Los Angeles, California 90095, USA

ARTICLE INFO

Article history:
Received 7 February 2022
Revised 3 August 2022
Accepted 28 August 2022

Keywords:
Dropwise condensation
Radiative coolers
Dew formation
Selective LWIR emittance
Broadband emittance

ABSTRACT

Dew formation occurs frequently on radiative cooling surfaces used for cooling of buildings and for harvesting atmospheric water as a result of dropwise condensation. The presence of these droplets can in turn alter the infrared emittance and performance of radiative cooling surfaces, in particular, selective emitters. This study experimentally investigates the impact of dropwise condensation on both the emittance and spectral selectivity of radiative cooling surfaces. Here, selective emitters supporting a large number of polydisperse acrylic droplets, as water droplet simulant, with contact angle ranging between 39° and 62° and surface area coverage between 20% and 52% were prepared and characterized. Spectral characterization revealed that the spectral emittance of the radiative cooling surfaces increased and broadened significantly in the presence of droplets. This was attributed to the absorption by the droplets. The emittance inside the long-wavelength infrared (LWIR) atmospheric transparency window increased slightly while the emittance outside increased significantly with increasing droplet surface area coverage and contact angle. This loss in spectral selectivity resulted in heat gain from radiation exchanges outside the LWIR, such that a given radiative cooling surface attained a higher temperature when covered with droplets. Dew formation may thus present important limitations on the performance achievable by selective emitters in radiative cooling applications.

1. Introduction

Passive radiative cooling is a natural phenomenon whereby sky-facing surfaces experience net radiative heat loss to the upper atmosphere and outer space due to a long-wavelength infrared (LWIR) atmospheric transmission window between 8 and 13 μm. In recent years, there has been significant growth in research efforts to exploit this phenomenon since it offers a "zero-energy" and "zero-carbon" way to cool terrestrial objects [1,2]. Such a passive method of cooling is being explored as a potential solution to meet cooling needs at the building-scale [3,4] and even potentially for geoengineering in order to combat climate change [5]. Radiative cooling of buildings can be achieved particularly via their rooftops for its advantageous view factor with the sky [6–8]. However, rooftop radiative cooling surfaces often collect dew at night, even in relatively arid regions [9]. Indeed, water droplets are commonly observed condensing on a radiative cooling surface as its temperature falls below the dew point temperature of the surrounding air [10–12], as illustrated in Fig. 1. As such, radiative cooling surfaces can also be used for harvesting atmospheric water by condensing atmospheric water vapor or fog [13,14]. Conversely, the presence of water droplets on radiative coolers may significantly alter the net infrared emittance of the radiative cooling surface and impact its cooling performance.

A widely acknowledged fact in radiative cooling research is that selective LWIR emitters, which preferentially emit their heat over wavelengths where the atmosphere is least emissive can in principle reach lower temperatures than a broadband emitter. This is because they can reduce non-LWIR radiative heat gain from the atmosphere [2,15]. Indeed, many recent works have emphasized the development of selective emitters for large-area outdoor applications [16], including planetary cooling [17]. However, these studies do not account for ambient phenomena like fog or dew condensation on emitters. Water is both a near-infrared absorber and a broadband thermal emitter [18]. Thus, dropwise condensation may

* Corresponding author.
E-mail address: pilon@seas.ucla.edu (L. Pilon).

https://doi.org/10.1016/j.ijheatmasstransfer.2022.123399

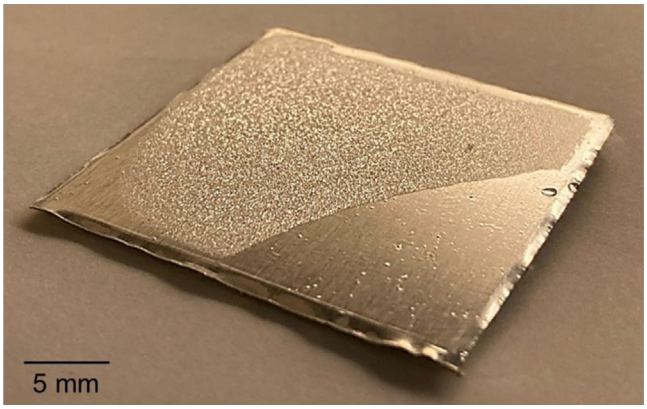

Fig. 1. Photograph illustrating dropwise water condensation on the selective radiative cooling surface investigated in this study. The lower right corner was wiped to better show the contrast.

Nomenclature

A	area (m^2)
d_p	droplet diameter (μm)
f_A	droplet surface area coverage (%)
k	absorption index
m	complex index of refraction, $m = n + ik$
n	refractive index
R	reflectance (%)
RH	relative humidity (%)
T	Temperature
T_{nh}	normal-hemispherical transmittance
T_{nn}	normal-normal transmittance
x	x coordinate of droplet center (mm)
y	y coordinate of droplet center (mm)

Greek Symbols

α	Absorptance
ε_d	total directional emittance
ε_n	total normal emittance
θ_c	droplet contact angle (°)
θ_i	angle (°)
λ	wavelength (nm)
σ	standard deviation in droplet size distribution

Subscription

a	refers to air
d	refers to droplet
dh	refers to directional-hemispherical
$LWIR$	refers to long-wavelength infrared
nh	refers to normal-hemispherical
s	refers to slab
λ	refers to spectral variables

broaden the narrowband emittances of the selective emitter and reduce their sub-ambient cooling power [2] and their supposed cooling benefits [16,17] over broadband emitters [8].

Trosseille et al. [19]. investigated experimentally the effect of dew formation on the total-hemispherical emittance of two different samples prepared to achieve high or low total normal emittance. The low emittance sample ($\varepsilon_n = 0.05$) consisted of an aluminum sheet whereas the high emittance sample ($\varepsilon_n = 0.88$) consisted of an aluminum sheet covered by a 250 μm thick polyvinyl chloride (PVC) sheet. Both samples were coated with a 6 μm thin film of low-density polyethylene (LDPE) so that the contact angle of water droplets on both samples was identical and equal to 65.9 ± 3.6° The experimental setup consisted of placing the sample on top of a copper block cooled with a Peltier element. An infrared camera working between 7.5 and 14 μm took thermography images to estimate the changes in total emittance as a function of time. At the beginning, both low and high emittance samples were dry and their emittance decreased slightly as they cooled down. As their temperature reached the dew point temperature of the surrounding air, dropwise condensation started and the surface emittance increased over time. This was attributed to the increase in the droplet diameter d_p and in the surface area coverage f_A. Eventually, both substrates' total-hemispherical emittance ε_n reached a steady-state value slightly lower than the emissivity of 0.98 corresponding to a semi-infinite layer of water. However, droplet diameter and surface area coverage of the samples during condensation as well as their spectral emittance were not reported. The study was complemented with a simple model for the total emissivity expressed as the sum of the emissivity of water and substrate weighted by their respective surface area coverage and experiments measuring the mass of condensate accumulated over time on a broadband radiative cooling surface exchanging with a cold enclosure. All measurements were performed indoor under controlled conditions (e.g., relative humidity, air, and substrate temperature).

Yang et al. [20]. used the Monte Carlo Ray Tracing (MCRT) method to numerically investigate infrared radiation transfer through a 0.1 mm thick polydimethylsiloxane (PDMS) film covered with water droplets. Monodisperse or polydisperse water droplets were arranged either in hexagonally or randomly on the front side of the surface with a normal incident angle. The droplet diameter d_p varied between 50 and 250 μm, contact angle θ_c between 10° and 180°, and projected surface area f_A between 5% and 90%. The cooling power of radiative cooling surfaces supporting droplets was calculated using the predicted transmittance. The authors recommended the use of superhydrophilic surfaces ($\theta_c = 10°$) to maximize the cooling power. Note that PDMS is a broadband emitter and that the numerical predictions were not validated against experimental data.

Unfortunately, to the best of our knowledge, the effects of dropwise condensation on the spectral selectivity and temperature of radiative cooling surfaces in response to radiation exchange with the universe background radiation through the atmosphere remain unexplored to date, in particular under actual outdoor sky conditions. Yet, it represents a fundamental challenge and limitation that the development and deployment of selective radiative cooling surfaces.

The objective of this study is to experimentally investigate the effect of dropwise condensation on the emittance, selectivity, and temperature of radiative cooling surfaces. To do so, a selective emitter recently proposed as a radiative cooling standard [21] supporting a large number of polydisperse acrylic droplets with different contact angles and surface area coverages were prepared and characterized. The spectral directional-hemispherical reflectance of the samples was measured in the infrared part of the electromagnetic spectrum. Then, the total directional emittance, directional emittance inside and outside the atmospheric transparency window of the dry and droplet-covered samples were calculated. Finally, outdoor nighttime experiments were conducted to compare the temperature reached by the dry and droplet-covered radiative cooling surfaces.

2. Materials and methods

2.1. Sample preparation

The reference radiative cooling surface used in this study consisted of 60 µm-thick 3 M Scotch™ Long-Lasting (SLL) tape (3 M,

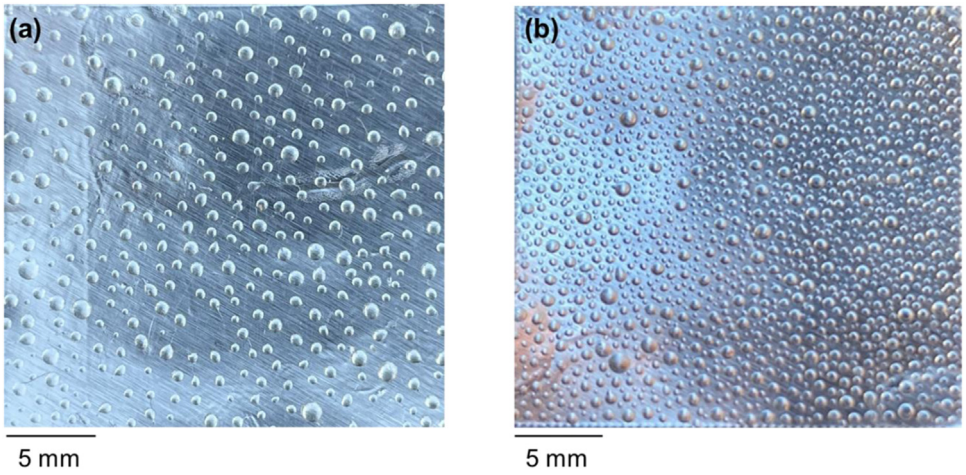

Fig. 2. Photograph of a reference sample supporting acrylic droplets with droplet mean contact angle $\bar{\theta}_c = 39°$ and surface area coverage (a) $f_A = 22\%$ and (b) $f_A = 50\%$.

USA) on 20 μm-thick aluminum (Al) foil with a surface area of 2.5 × 2.5 cm^2. Samples were prepared by applying two layers of scotch tape manually onto the Al foil, with care taken to prevent the formation of air bubbles below and between the layers. A total of nine different samples with or without hydrophobic coatings were prepared to achieve different droplet contact angles and projected surface area coverages including (1) the reference surface with droplet surface area coverage f_A ranging between 0% and 100% (Samples 1–5), (2) the reference surface coated with commercial water-repellent spray paint (NeverWet™, Rust-Oleum, USA) with f_A ranging between 0% and 51% (Samples 6, 7A, 7B), and (3) the reference surface coated with monolayer of perfluorinated silane (tridecafluoro-1,1,2,2,-tetrahydrooctyl)trichlorosilane (Gelest, USA) with f_A ranging between 0% and 52% (Samples 8, 9, 10A, 10B). The reference sample was used to represent the hydrophilic radiative cooling surface while NeverWet™ and perfluorinated silane coated samples were representatives of hydrophobic radiative cooling surfaces.

Samples 6 and 7 were made by coating the reference surface with water-repellent spray paint. First, NeverWet™ Step 1 Base Coat (275,185) was sprayed directly on the sample surface and dried for one hour. Then, NeverWet™ Step 2 Top Coat (275,185) was sprayed again onto the surface of the sample and left to dry for 12 h. Samples 8, 9, 10A, and 10B were prepared by coating the reference surface with perfluorinated silane. To do so, samples were placed inside a closed container with liquid perfluorinated silane. The silane vaporized and reacted with hydroxyl groups (–OH) present on the cellulose acetate - the main group of the non-sticking side of the SLL tape - and formed a hydrophobic coating [22].

Lastly, thousands of droplets made of acrylic polymer (Loctite AA 349, Henkel Adhesives, USA) were deposited manually on the surface of the uncoated and coated samples. The tip of the needle of a syringe was used to deposit liquid acrylic droplets from the acrylic container onto the radiative cooling surfaces. This procedure was repeated until the desired droplet surface area coverage f_A was achieved. After the deposition, acrylic droplets were cured with a UV lamp (Blak-Ray B-100A, Thermo Scientific Fisher, USA) emitting at a wavelength of 365 nm. Fig. 2 shows the photograph of the reference sample supporting acrylic droplets with droplet mean contact angle $\bar{\theta}_c = 39°$ and surface area coverage (a) $f_A = 22\%$ (Sample 3) and (b) $f_A = 50\%$ (Sample 5). In addition, Sample 2 consisted of an acrylic film 300 μm in thickness deposited on the reference surface using a film applicator (EQ-Se-KTQ-150, MTI Corporation, USA) to achieve a surface area coverage $f_A = 100\%$ to serve as a reference. Polymer droplets rather than water droplets were used to eliminate any change in the droplet diameter and surface area coverage during the deposition and measurements caused by evaporation, rolling off, and/or merging of the droplets. As a result, the droplet size distribution and surface area coverage of each sample remained constant and could be thoroughly characterized. Acrylic droplets could serve as a simulant of water droplets on the basis that both acrylic and water are transparent in the visible and near-infrared for wavelengths up to 1 μm and are broadband thermal emitters in the infrared. Therefore, the optical effects caused by the presence of the acrylic droplets are expected to be those of water droplets despite the difference in their refractive and absorption indices. The validity of this approach is rigorously demonstrated in Section 3.

2.2. Droplet characterization

The contact angle of the acrylic droplets deposited on the uncoated and coated radiative cooling surfaces was measured with a goniometer (VCA-3000S, AST Products, USA). The mean droplet contact angle $\bar{\theta}_c$ was measured by averaging the contact angle measurements for at least 5 droplets. The images of droplet-covered samples were captured with a camera and analyzed with ImageJ (National Institutes of Health, USA) to determine the droplet surface area coverage f_A and the mean projected diameter $\bar{d}_p$ and standard deviation σ.

2.3. Infrared characterization

A nitrogen-purged Fourier transform infrared (FTIR) spectrometer (Nicolet™ iS50, Thermo Scientific Fischer, USA) equipped with an integrating sphere (Upward IntegratIR™, PIKE Technologies, USA) was used to measure the spectral normal-hemispherical reflectance $R_{nh,\lambda}$ of the dry and droplet-covered samples. The spectral directional-hemispherical reflectance $R_{dh,\lambda}$ of the samples were measured using a FTIR spectrometer (INVENIO®, Bruker) equipped with a custom-made integrating sphere. For both measurements, a potassium bromide (KBr) beamsplitter and a liquid-nitrogen cooled mercury-cadmium-telluride (MCT) detector were used in the spectral range between 2 and 20 μm. Note that, the atmospheric transmission window between 16 and 22 μm may be transparent but only for very low total precipitable atmospheric water levels, and even then, its contribution to the radiative cooling is relatively small [2,23]. Therefore, this spectral window was not taken into consideration in this study.

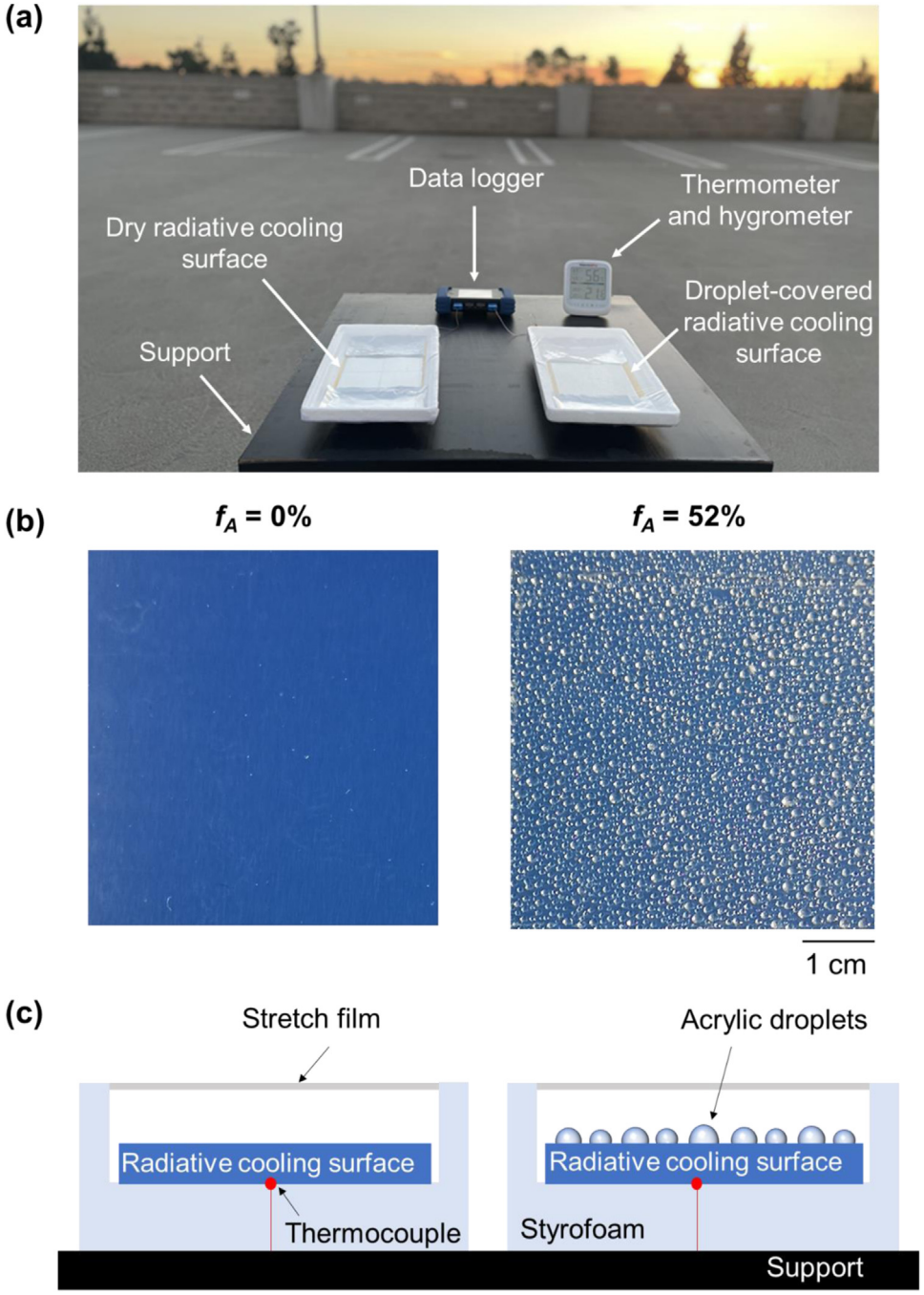

Fig. 3. Photographs of the (a) experimental setup and of (b) uncoated dry and droplet-covered radiative cooling surfaces. (c) Schematic of the setup used in the outdoor nighttime experiments.

2.3.1. Spectral directional emittance

For opaque surfaces, the spectral directional emittance $\varepsilon_{d,\lambda}$ is given by Kirchhoff's law expressed as [24]

$$\varepsilon_{d,\lambda} = \alpha_{d,\lambda} = 1 - R_{dh,\lambda} \tag{1}$$

where $\alpha_{d,\lambda}$ is the spectral directional absorptance and $R_{dh,\lambda}$ is the directional-hemispherical reflectance. Note that, the directional spectral emittance in the normal direction $\theta_i = 0°$ is equal to the normal spectral emittance denoted by $\varepsilon_{n,\lambda}$, i.e. $\varepsilon_{d,\lambda}(\theta_i = 0°) = \varepsilon_{n,\lambda}$.

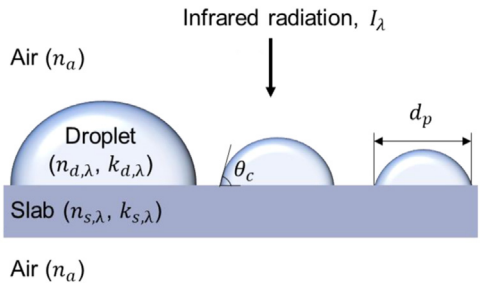

Fig. 4. Schematic of a simulated horizontal semi-infinite opaque slab supporting polydisperse droplets on its front side.

Table 1
Emittances of the simulated glass and aluminum substrates dry or covered with acrylic or water droplets with surface area coverage f_A = 52% and projected diameter $\bar{d}_p \pm \sigma$ = 412 ± 212 μm.

Surface	Droplet	θ_c (°)	ε_n (-)	$\varepsilon_{n,LWIR}$ (-)
Dry glass	N/A	N/A	0.91	0.87
Droplet-covered glass	Acrylic	30	0.93	0.91
Droplet-covered glass	Acrylic	60	0.94	0.92
Droplet-covered glass	Acrylic	90	0.94	0.92
Droplet-covered glass	Water	30	0.95	0.92
Droplet-covered glass	Water	60	0.95	0.93
Droplet-covered glass	Water	90	0.95	0.93
Dry aluminum	N/A	N/A	0.01	0.01
Droplet-covered aluminum	Acrylic	30	0.37	0.45
Droplet-covered aluminum	Acrylic	60	0.47	0.49
Droplet-covered aluminum	Acrylic	90	0.46	0.47
Droplet-covered aluminum	Water	30	0.48	0.49
Droplet-covered aluminum	Water	60	0.49	0.49
Droplet-covered aluminum	Water	90	0.48	0.48

2.3.2. Total directional emittance

The total directional emittance ε_d can be calculated according to [24]

$$\varepsilon_d = \frac{\int_0^\infty \varepsilon_{d,\lambda} E_{b,\lambda}(T_o) d\lambda}{\int_0^\infty E_{b,\lambda}(T_o) d\lambda} \approx \frac{\int_{2\ \mu m}^{20\ \mu m} \varepsilon_{d,\lambda} E_{b,\lambda}(T_o) d\lambda}{\int_{2\ \mu m}^{20\ \mu m} E_{b,\lambda}(T_o) d\lambda} \quad (2)$$

where $E_{b,\lambda}(T_o)$ is the blackbody spectral emissive power (in W/m^2·μm) at temperature T_o = 296 K. The integrals in both the numerator and denominator of Eq. (2) were truncated to wavelengths between 2 - 20 μm as the samples were opaque in this spectral range. Here also, the total directional emittance ε_d in the normal direction $\theta_i = 0°$ is the total normal emittance denoted by ε_n so that $\varepsilon_d(\theta_i = 0°) = \varepsilon_n$.

2.3.3. Directional emittance inside and outside the atmospheric window

The directional emittance $\varepsilon_{d,LWIR}$ inside the atmospheric transparency window, defined by the wavelength range between 8 - 13 μm [23], was defined as [2]

$$\varepsilon_{d,LWIR} = \frac{\int_{8\ \mu m}^{13\ \mu m} \varepsilon_{d,\lambda} E_{b,\lambda}(T_o) d\lambda}{\int_{8\ \mu m}^{13\ \mu m} E_{b,\lambda}(T_o) d\lambda}. \quad (3)$$

Similarly, the directional emittance outside the atmospheric transparency window $\varepsilon_{d,non\text{-}LWIR}$ can be expressed as [2]

$$\varepsilon_{d,non-LWIR} = \frac{\int_{2\ \mu m}^{20\ \mu m} \varepsilon_{d,\lambda} E_{b,\lambda}(T_o) d\lambda - \int_{8\ \mu m}^{13\ \mu m} \varepsilon_{d,\lambda} E_{b,\lambda}(T_o) d\lambda}{\int_{2\ \mu m}^{20\ \mu m} E_{b,\lambda}(T_o) d\lambda - \int_{8\ \mu m}^{13\ \mu m} E_{b,\lambda}(T_o) d\lambda} \quad (4)$$

2.4. Outdoor nighttime temperature measurements

Outdoor nighttime experiments were conducted to assess the effect of droplets on the temperature of the radiative cooling surface under actual outdoor conditions. The experiments were performed at night to prevent differences in solar absorptance of the dry and droplet-covered samples from interfering with any differential cooling arising from the differential thermal emittance. Fig. 3(a) shows the experimental setup consisting of (i) dry and droplet covered samples used for outdoor experiments with a surface area of A = 10×10 cm^2, (ii) a data logger (RDXL6SD-USB, OMEGA Engineering, USA) used to record the temporal evolution of the samples' temperature, and (iii) a thermometer with ±1 °C accuracy combined with a hygrometer with ±3% accuracy (TP59, ThermoPro, USA) to measure the temperature and relative humidity (RH) of the ambient air.

Two different samples, shown in Fig. 3(b), were prepared for outdoor experiments including a dry and a droplet-covered sample with droplet contact angle $\bar{\theta}_c$ = 39° and surface area coverage f_A = 52%. Samples were placed in an open-top Styrofoam casing to ensure thermal insulation from the horizontal support, as schematically illustrated in Fig. 3(c). In addition, the top surface of the casing was covered with a 10 μm thick infrared transparent low-density poly(ethylene) (PE) film (see Figure S1 in Supplementary Material) to limit convective heat transfer. A calibrated T-type thermocouple (OMEGA Engineering, USA) with ±1 °C accuracy was placed at the bottom of the sample and sealed with thermal tape. All experiments were conducted at nighttime on the rooftop of a parking lot in Los Angeles, California so that horizontal samples had an unobstructed view of the sky and on different months (April 28, May 21, September 1, and October 12, 2021) with different sky and humidity conditions to explore a wide range of realistic situations.

3. Analysis

In order to justify the use of acrylic droplets as a substitute for water droplets in terms of optics and thermal emissions, two different approaches were followed. First, the spectral normal emissivities of a semi-infinite slab made from acrylic or water were calculated and compared. Second, the spectral normal emittance of a slab supporting polydisperse acrylic or water droplets on its front side was numerically predicted using the Monte Carlo ray-tracing (MCRT) method previously developed [25,26] and experimentally validated in the visible [27] and infrared [28] parts of the electromagnetic spectrum.

First, the normal spectral emissivity $\varepsilon_{n,s,\lambda}$ of an optically smooth semi-infinite slabs made of acrylic or water was calculated using Equation (S1). Figure S2 in Supplementary Materials compares the spectral normal emissivity $\varepsilon_{n,\lambda}$ of acrylic and water for wave-

Table 2
Summary of the characteristics of the dry and acrylic droplet-covered radiative cooling samples used in this study.

Sample #	Surface treatment	$\bar{\theta}_c$ (°)	f_A (%)	$\bar{d}_p \pm \sigma$ (μm)	ε_n (-)	$\varepsilon_{n,LWIR}$ (-)	$\varepsilon_{n,non-LWIR}$ (-)
1	None	N/A	0	–	0.69	0.88	0.54
2	None	N/A	100	300 (film)	0.95	0.96	0.94
3	None	39.0 ± 2.9	22 ± 5	541 ± 158	0.74	0.89	0.62
4	None	39.0 ± 2.9	40 ± 5	417 ± 163	0.79	0.90	0.69
5	None	39.0 ± 2.9	50 ± 5	384 ± 166	0.81	0.91	0.72
6	NeverWet™	50.2 ± 1.4	0	–	0.75	0.89	0.63
7A	NeverWet™	50.2 ± 1.4	40 ± 5	711 ± 212	0.81	0.91	0.73
7B	NeverWet™	50.2 ± 1.4	51 ± 5	575 ± 293	0.83	0.92	0.75
8	silane	62.3 ± 4.0	0	–	0.71	0.88	0.57
9	silane	62.3 ± 4.0	20 ± 5	462 ± 137	0.76	0.90	0.66
10A	silane	62.3 ± 4.0	40 ± 5	475 ± 196	0.81	0.91	0.73
10B	silane	62.3 ± 4.0	52 ± 5	412 ± 212	0.84	0.93	0.77

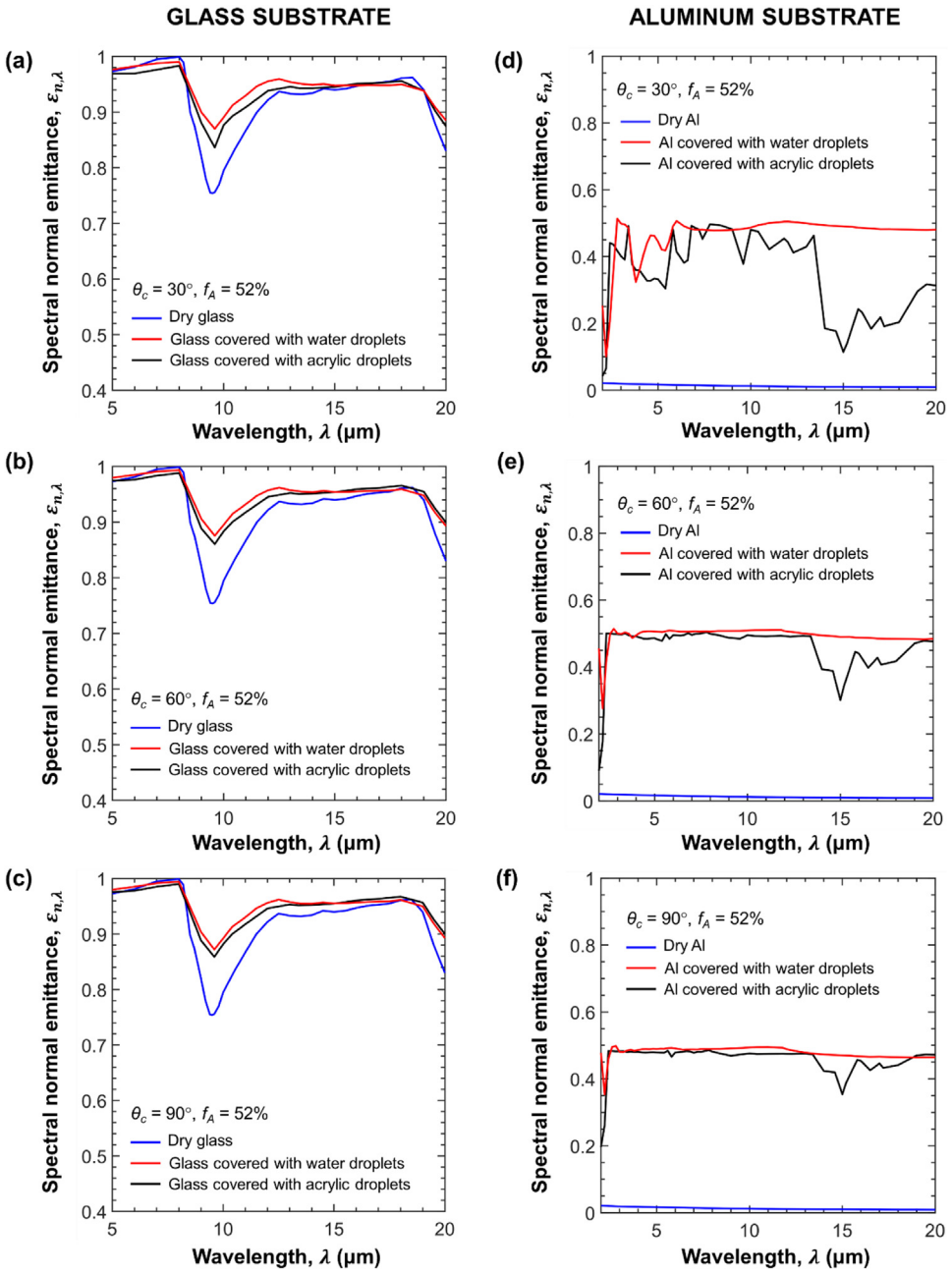

Fig. 5. Spectral normal emittance $\varepsilon_{n,\lambda}$ of (a, b, c) glass and (d, e, f) aluminum substrates dry or covered with water or acrylic droplets with f_A = 52% and (a, d) θ_c = 30°, (b, e) θ_c = 60°, and (c, f) θ_c = 90°.

lengths λ between 2.4 μm and 20 μm. It indicates that both water and acrylic have large emissivity exceeding 0.93 across the spectral window considered. Water had a spectral emittance $\varepsilon_{n,\lambda}$ within 1–6% of that acrylic across this spectral window (see Figure S3 in Supplementary Materials). The total normal emissivities ε_n of the water and acrylic were both large, similar, and equal to 0.97 and 0.96, respectively. In addition, the total normal emissivities $\varepsilon_{n,LWIR}$ inside the atmospheric transparency window of the water and acrylic slabs were 0.99 and 0.96, respectively. In addition, the ratio of the total normal emissivity inside and outside the atmospheric transparency window ($\varepsilon_{n,LWIR}/\varepsilon_{n,non\text{-}LWIR}$) for water and acrylic were near unity, indicating that both water and acrylic are broadband emitters.

Second, Fig. 4 shows the schematic of an opaque slab with a complex refractive index $m_{s,\lambda} = n_{s,\lambda} + ik_{s,\lambda}$ supporting polydisperse droplets on its front side with contact angle θ_c, projected diameter d_p, and complex refractive index $m_{d,\lambda} = n_{d,\lambda} + ik_{d,\lambda}$. The droplet-covered surface is exposed to collimated and normally incident infrared radiation intensity I_λ at wavelength λ. In order to simulate realistic droplet size and surface area coverage f_A, the projected diameter d_p and coordinates (x, y) of 528 droplets deposited and characterized on Sample 10B with f_A = 52% were used in the numerical simulations. Two different surfaces were simulated namely soda-lime glass surface due to its high emissivity and aluminum surface due to its low emissivity [24]. The spectral refractive $n_{s,\lambda}$ and absorption $k_{s,\lambda}$ indices of the slab made from soda-lime glass and aluminum were taken from Refs [29,30], respectively. Similarly, the spectral refractive $n_{d,\lambda}$ and absorption $k_{d,\lambda}$ indices of the droplets made from acrylic and water were taken from Refs [18,31], respectively (see Figure S4 in Supplementary Material).

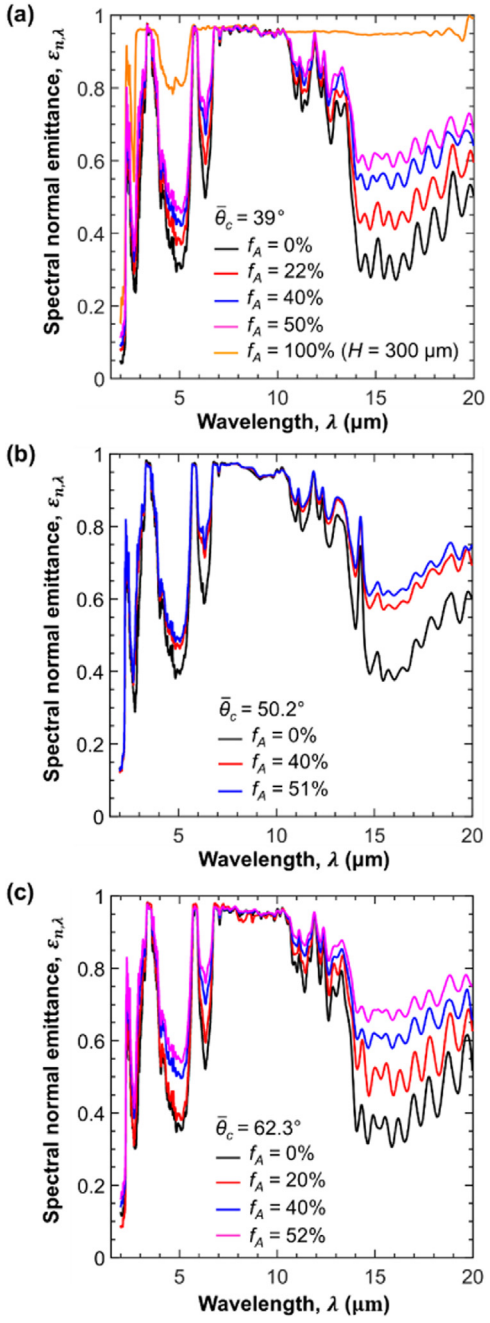

Fig. 6. Spectral normal emittance $\varepsilon_{n,\lambda}$ as a function of wavelength λ for dry sample (Sample 1), sample covered with 300 mm thick acrylic film (Sample 2), and droplet-covered samples with (a) contact angle $\bar{\theta}_c = 39°$ and surface area coverage f_A between 22% and 50% (Samples 3 - 5), (b) $\bar{\theta}_c = 50.2°$ and f_A between 0% and 51% (Samples 6 - 7B), and (b) $\bar{\theta}_c = 62.3°$ and f_A between 0% and 52% (Samples 8 - 10B).

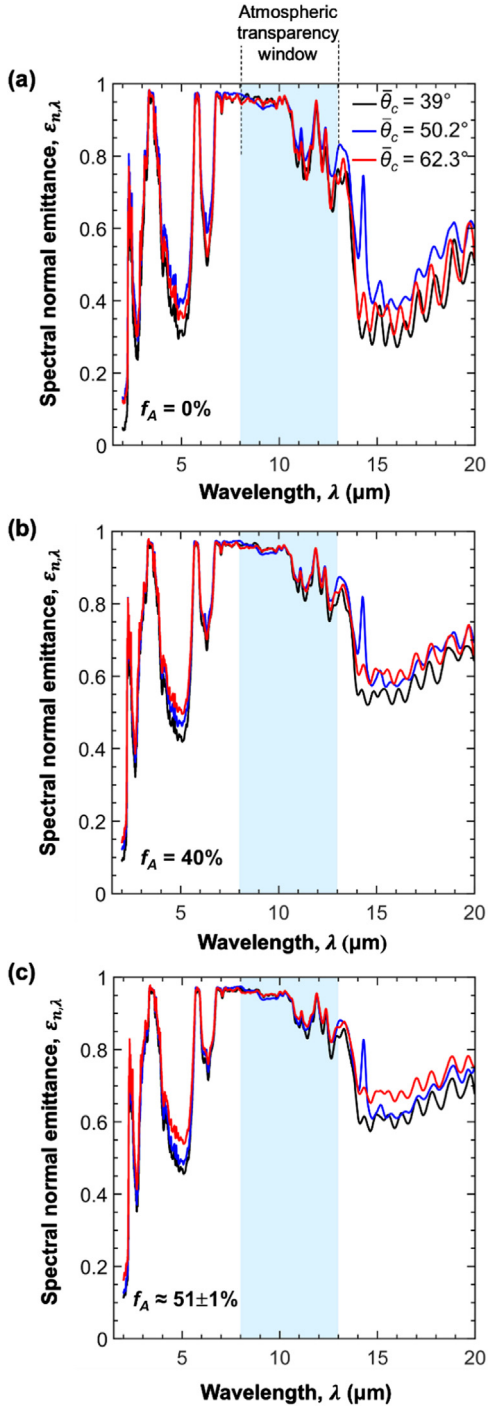

Fig. 7. Spectral normal emittance $\varepsilon_{n,\lambda}$ for (a) dry samples (Samples 1, 6, 8) and droplet-covered samples with contact angle $\bar{\theta}_c = 39°$, 50.2°, and 62.3° and surface area coverage, (b) $f_A = 40\%$ (Samples 4, 7A, and 10A), and (c) $f_A \approx 51 \pm 1\%$ (Samples 5, 7B, and 10B).

The normal-hemispherical reflectance $R_{nh,\lambda}$ of the opaque substrate supporting acrylic or water droplets on its front side was numerically predicted using the Monte Carlo ray-tracing (MCRT) method described in Ref [26]. The same assumptions were used including (1) all interfaces were optically smooth such that Fresnel equation and Snell's law were valid. (2) All droplets were cap-shaped with identical contact angle θ_c and constant curvature. (3) The droplet size and slab dimensions were much larger than the wavelength λ of the infrared radiation I_λ such that geometric optics prevailed. Here, 10^6 photon bundles were used in each simulation to achieve numerical convergence. After determining the normal-hemispherical reflectance $R_{nh,\lambda}$, the spectral emittance $\varepsilon_{n,s,\lambda}$ of the droplet covered slabs was calculated from Eq. (1).

Fig. 5 shows the spectral normal emittance $\varepsilon_{n,\lambda}$ of the soda-lime glass substrate dry or covered with acrylic or water droplets on their front side with contact angle (a) $\theta_c = 30°$, (b) $\theta_c = 60°$, and (c) $\theta_c = 90°$, surface area coverage $f_A = 52\%$, and projected diameter $\bar{d}_p \pm \sigma = 412 \pm 212$ μm for wavelengths λ between 5 μm and 20 μm. Figs. 5(a) - 5(c) indicate that the emittance $\varepsilon_{n,\lambda}$ of

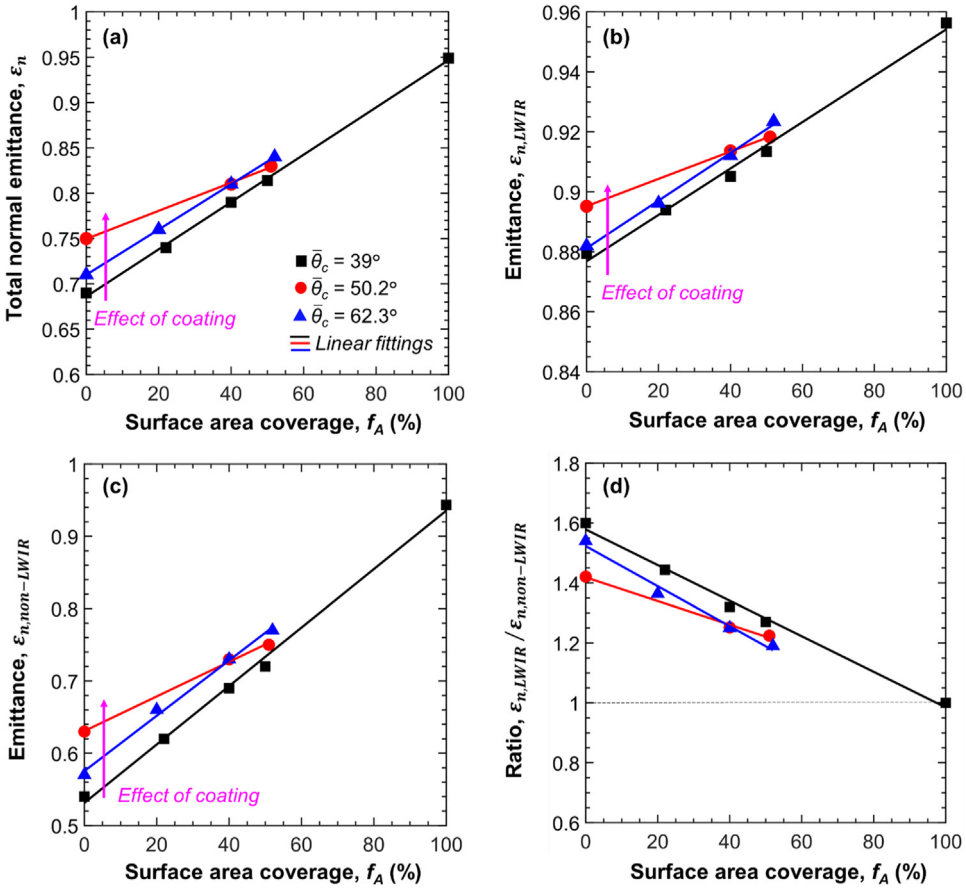

Fig. 8. (a) Total normal emittance ε_n (b) normal emittance $\varepsilon_{n,LWIR}$ inside the atmospheric transparency window, (c) normal emittance $\varepsilon_{n,non-LWIR}$ outside the atmospheric transparency window, and (d) ratio of the emittance $\varepsilon_{n,LWIR}/\varepsilon_{n,non-LWIR}$ as functions of surface area coverage f_A for contact angles $\bar{\theta}_c$= 39°, 50.2°, and 62.3°.

the dry glass increased slightly in the presence of acrylic or water droplets. In addition, it shows that the glass surface had slightly larger emittance $\varepsilon_{n,\lambda}$ when covered with water droplets than with acrylic droplets for droplet contact angle $\theta_c = 30°$. However, for $\theta_c = 60°$ and 90°, the emittances $\varepsilon_{n,\lambda}$ of the glass surfaces supporting water or acrylic droplets were nearly identical and fell within 2% of each other. This was due to the fact that absorption of the radiation by the acrylic droplets increased with increasing contact angle θ_c as the droplet volume increased.

Fig. 5 also plots the spectral normal emittance $\varepsilon_{n,\lambda}$ of the aluminum substrate dry or supporting acrylic or water droplets on their front side with (d) $\theta_c = 30°$, (e) $\theta_c = 60°$, and (f) $\theta_c = 90°$, f_A = 52%, and $\bar{d}_p \pm \sigma$ = 412 ± 212 μm for wavelengths λ between 2 μm and 20 μm. These figures indicate that the emittance $\varepsilon_{n,\lambda}$ of the dry aluminum increased drastically in the presence of the strongly and broadband emitting acrylic or water droplets. It also indicates that aluminum had larger spectral emittance $\varepsilon_{n,\lambda}$ when covered with water droplets than with acrylic droplets for $\theta_c = 30°$. However, the differences in emittance $\varepsilon_{n,\lambda}$ with acrylic or water droplets decreased with increasing contact angle θ_c.

Table 1 summarizes the total normal emittance ε_n and the emittance $\varepsilon_{n,LWIR}$ inside the atmospheric transparency window of the glass and aluminum substrates dry or covered with acrylic or water droplets with contact angle $\theta_c = 30°$, 60°, 90°, f_A = 52%, and $\bar{d}_p \pm \sigma$ = 412 ± 212 μm. Overall, these results demonstrate that the effects caused by the presence of acrylic droplets on the spectral and total emittances of radiative cooling surfaces were similar to that of water droplets. Thus, acrylic droplets can be used as a simulant of water droplets in the infrared.

4. Results and discussion

4.1. Sample characterization

Table 2 summarizes the mean droplet contact angle $\bar{\theta}_c$, projected diameter d_p, and surface area coverage f_A of the dry and droplet-covered samples investigated in this study. The droplet mean contact angle was (i) $\bar{\theta}_c$= 39.0 ± 2.9° for the uncoated reference Samples 1–5, (ii) $\bar{\theta}_c$= 50.2 ± 1.4° for Samples 6–7B coated with NeverWet™, and (iii) $\bar{\theta}_c$= 62.3 ± 4.0° for Samples 8–10B coated with perfluorinated silane. The droplet contact angle measurements of the different samples are reported in Figure S5 in Supplementary Materials. The droplet surface area coverage f_A of the droplet-covered samples ranged between 20% and 52% while the droplet mean diameter ranged between 384 μm and 711 μm. During dropwise condensation on a cold substrate, droplets feature a broad size distribution whose maximum falls within the reported range of diameter of our experiments [24,32,33]. In addition, experiments on condensation on vertical windows [34] showed that the maximum surface area coverage was about 55% for a wide range of contact angle due to droplet sliding under gravity and coalescing.

In addition, the droplet diameter was shown to have a negligible effect on the emittance of glass or aluminum substrate for surface coverage f_A = 25% and 50%, and droplet contact angle and diameter in the range considered in this study (see Figure S6 in Supplementary Material). This can be attributed to the fact that sufficiently large droplets could be treated as opaque in the infrared. Note that for low droplet contact angles, the droplets were small and semitransparent, and the emittance of the aluminum

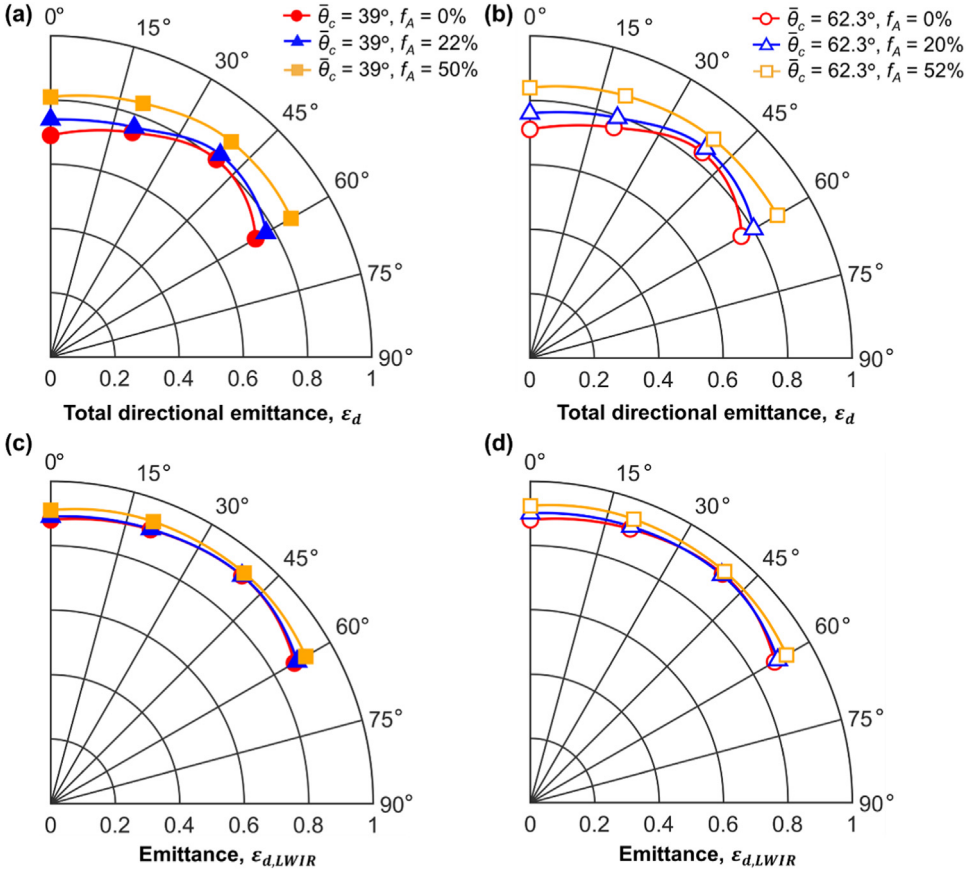

Fig. 9. (a, b) Total directional emittance ε_d and (c, d) directional emittance in the atmospheric transparency window $\varepsilon_{d,LWIR}$ as functions of angle θ_i for dry and droplet-covered samples with $\bar{\theta}_c$= 39°and 62.3° and surface area coverage between f_A = 0% and 52%.

substrate supporting droplets increased from 0.2 to 0.45 with increasing droplet diameter between 50 and 600 μm for f_A = 50%.

4.2. Infrared characterization

4.2.1. Spectral normal emittance

Fig. 6 plots the spectral normal emittance $\varepsilon_{n,\lambda}$ between 2 and 20 μm for the dry radiative cooling surface (Sample 1), the sample covered with a 300 mm thick acrylic film (Sample 2), and acrylic droplet-covered samples with (a) $\bar{\theta}_c$ = 39° and f_A = 22, 40, and 50% (Samples 3, 4, 5), (b) $\bar{\theta}_c$ = 50.2° and f_A = 0, 40, and 51% (Samples 6, 7A, 7B), and (c) $\bar{\theta}_c$ = 62.3° and f_A = 0, 20, 40, and 52% (Samples 8, 9, 10A, 10B). Fig. 6(a) shows that the reference sample (Sample 1) had a high spectral normal emittance $\varepsilon_{n,\lambda}$ in the atmospheric transparency window (8 μm $\leq \lambda \leq$ 13 μm) while it featured a lower emittance $\varepsilon_{n,\lambda}$ in the rest of the spectrum. It establishes that the dry reference sample was a selective emitter. Fig. 6 indicates that increasing the droplet surface area coverage f_A increased the emittance $\varepsilon_{n,\lambda}$ for any given contact angle considered. This was attributed to the fact that the number of photons absorbed by the acrylic droplets increased as the droplet surface area coverage f_A and the volume of droplets deposited increased. Note that the presence of droplets did not significantly increase the spectral normal emittance $\varepsilon_{n,\lambda}$ for wavelength λ between 7 and 11 μm as the dry sample already featured a large emittance. In addition, Fig. 6(a) shows that for surface area coverage f_A = 100% the spectral normal emittance $\varepsilon_{n,\lambda}$ was constant and approached unity for wavelengths $\lambda \geq$ 6 μm.

Fig. 7 plots the spectral normal emittance $\varepsilon_{n,\lambda}$ as a function of wavelength λ for the dry and droplet-covered samples with droplet contact angles $\bar{\theta}_c$ ranging from 39° to 62.3° and surface area coverage (a) f_A = 0% (Sample 1, 6, 8), (b) f_A = 40% (Sample 3, 7A, 10A), and (c) $f_A \approx$51 $\pm$ 1% (Sample 4, 7B, 10B). Fig. 7(a) indicates that the presence of silane coating did not affect significantly the spectral normal emittance $\varepsilon_{n,\lambda}$ of the reference sample. By contrast, the spectral normal emittance $\varepsilon_{n,\lambda}$ of the reference sample increased for $\lambda \geq$ 13 μm when coated with NeverWet^{TM}. Moreover, Figs. 7(b) and 7(c) indicate that, for a given surface area coverage f_A, the spectral normal emittance $\varepsilon_{n,\lambda}$ increased as the droplet contact angle $\bar{\theta}_c$ increased from 39° to 62.3°. This was attributed to absorption by the droplets since the volume of the droplets increased with increasing contact angle $\bar{\theta}_c$.

4.2.2. Total and LWIR normal emittance

Fig. 8 plots the calculated (a) total normal emittance ε_n, (b) normal emittance $\varepsilon_{n,\ LWIR}$ inside the atmospheric transparency window, (c) normal emittance $\varepsilon_{n,\ non-LWIR}$ outside the atmospheric transparency window, and (d) ratio of $\varepsilon_{n,\ LWIR}$ to $\varepsilon_{n,\ non-LWIR}$ as functions of surface area coverage f_A for dry sample (Sample 1), sample covered with 300 mm thick acrylic film (Sample 2), and droplet-covered samples with droplet contact angle $\bar{\theta}_c$ = 39° (Samples 3, 4), $\bar{\theta}_c$ = 50.2° (Samples 5, 6, 7A, 7B), and $\bar{\theta}_c$ = 62.3° (Samples 8, 9, 10A, 10B). Fig. 8(a) indicates that the total normal emittance ε_n [Eq. (2) for θ_i = 0°] increased almost linearly with increasing droplet surface area coverage f_A for all droplet contact angles considered, as illustrated with the solid line connecting the emittance for Samples 1 and 2. This was attributed to the fact that absorption by the droplets increased with increasing surface area coverage f_A. In addition, Fig. 8(b) indicates that the emittance $\varepsilon_{n,\ LWIR}$ inside the atmospheric transparency window in-

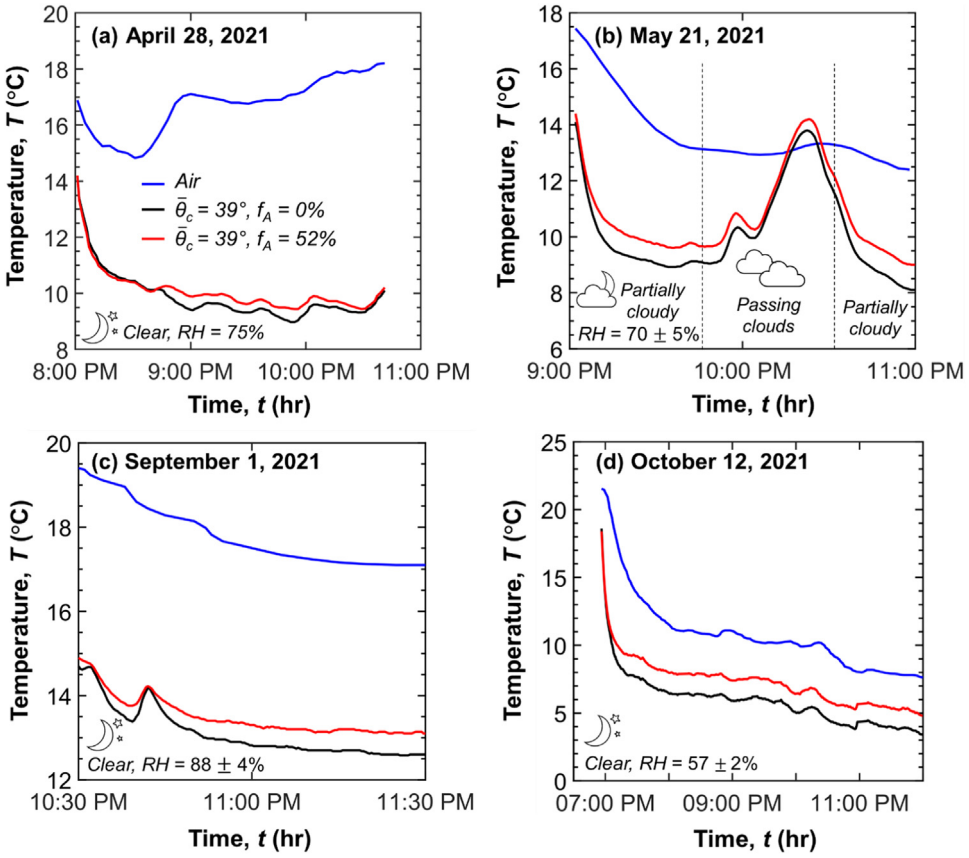

Fig. 10. Temperature T as a function of time t of the dry (f_A = 0%) and droplet-covered sample with contact angle $\bar{\theta}_c$ = 39° and f_A = 52% at different days.

creased slightly in the presence of droplets from the already large emittance $\varepsilon_{n,\ LWIR}$ = 0.88 of the dry sample. Fig. 8(c) shows that the normal emittance $\varepsilon_{n,\ non-LWIR}$ outside the atmospheric transparency window [Eq. (4) for θ_i = 0°] increased significantly with increasing surface area coverage f_A. Such an increase in $\varepsilon_{n,\ non-LWIR}$ is not desirable as it increases the absorption of radiation from the surrounding [2]. Table 2 summarizes the total normal emittance ε_n, the emittance $\varepsilon_{n,LWIR}$ inside and $\varepsilon_{n,non-LWIR}$ outside the atmospheric transparency window of the samples used in this study.

Figs. 8(a) and 8(b) also show that the presence of the NeverWet™ and silane coatings on dry samples (f_A = 0%) resulted in larger emittances ε_n and $\varepsilon_{n,\ LWIR}$ than the uncoated reference Sample 1 (see Table 2). This could be due to the fact that the silane ($\bar{\theta}_c$= 62.3°) and NeverWet™ ($\bar{\theta}_c$= 50.2°) coatings applied on the samples are themselves either broadband emissive or may have an antireflection effect. Moreover, to evaluate the selectivity of the radiative emitters [35], Fig. 8(d) plots the ratio of emittances inside and outside the atmospheric transparency window [$\varepsilon_{n,\ LWIR}/\varepsilon_{n,non-LWIR}$]. It indicates that $\varepsilon_{n,\ LWIR}/\varepsilon_{n,\ non-LWIR}$ decreased due to the presence of droplets and reached unity for f_A = 100%.

4.2.3. Total and LWIR directional emittances

Fig. 9 shows the measured (a, b) total directional emittance ε_d and (c, d) directional emittance $\varepsilon_{d,LWIR}$ inside the atmospheric transparency window as functions of angle θ_i for the dry and droplet-covered samples with (a, c) $\bar{\theta}_c$ = 39° and f_A ranging from 0% to 50% (Sample 1, 3, 5) and (b, d) $\bar{\theta}_c$ = 62.3° and f_A between 0% and 52% (Sample 8, 9, 10B). The spectral directional emittances $\varepsilon_{d,\lambda}$ at angles θ_i = 0°, 20°, 40°, and 60° used to compute ε_d and $\varepsilon_{d,LWIR}$ are reported in Figure S7 in Supplementary Materials. Figs. 9(a) and 9(b) indicate that the total directional emittance ε_d of the dry and droplet-covered samples initially increased slightly with increasing angle θ_i to reached a maximum around θ_i = 40°. These results are qualitatively consistent with measurements reported by Huang et al. [21] for the dry reference sample. This behavior can be attributed to two competing effects namely (i) the surface reflectivity increased with increasing angle θ_i and (ii) the emittance increased with angle θ_i due to the increase in optical thickness of the emissive SLL tape. In addition, the total directional emittance ε_d increased with increasing surface area coverage f_A for all angles θ_i considered due to absorption by the droplets. However, Figs. 9(c) and 9(d) show that the directional emittance inside the atmospheric transparency window $\varepsilon_{d,LWIR}$ increased slightly in the presence of droplets as the reference sample had large $\varepsilon_{d,LWIR}$ even at larger angles.

4.3. Outdoor nighttime temperature measurements

Fig. 10 shows the measured temperature T of the dry and droplet-covered samples as a function of time t for $\bar{\theta}_c$ = 39° and f_A = 52% on (a) April 28, (b) May 21, (c) September 1, and (d) October 12, 2021. It confirms that the dry and droplet-covered samples had a lower temperature than the air due to radiative cooling under clear sky and partially cloudy conditions. However, under cloud coverage, the surface temperature was larger than that of air, as observed in Fig. 10(b). This could be attributed to the fact that the clouds obstructed the view of the sky so that radiation exchanges occurred between the samples and the clouds that were warmer than the clear sky, resulting in a higher surface temperature. Moreover, Fig. 10 indicates that the dry sample had a systematically lower temperature than the droplet-covered sample with a temperature difference up to 1.7 °C, as illustrated in Fig. 10(d).

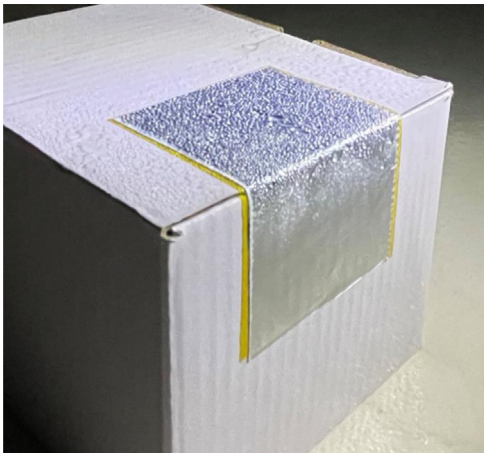

Fig. 11. Photograph of the selective emitter taped on a broadband emitter paper box, taken on a humid night in Los Angeles (September 28, 2021, 02:00 AM, T_a = 16 °C, RH = 88%).

This can be attributed to the higher selectivity of the dry sample, which prevents undesirable heat gain from the relatively warm atmosphere. Although the dry sample was a selective emitter, it acted as a broadband emitter in the presence of the droplets, as previously explained. In the absence of convective heat transfer and solar irradiance, the steady-state temperature of the radiative cooling surface given by [24]

$$T = \left(\frac{\alpha_{atm}}{\varepsilon_n}\frac{G_{atm}}{\sigma}\right)^{1/4}. \quad (5)$$

Here, σ (=5.67×10^{-8} W/m^2/K^4) is the Stefan-Boltzmann constant and α_{atm} is the total absorptance under irradiation G_{atm} reaching the surface from the atmospheric emission. The latter is expressed as

$$G_{atm} = \sigma T_{sky}^4 \quad (6)$$

where T_{sky} is the effective sky temperature ranging from 230 K to 285 K depending on the weather conditions [24]. The ratio of the total absorptance to the emittance ($\alpha_{atm}/\varepsilon_n$) determines the temperature T of the radiative cooling surface and increases in presence of droplets, as explained earlier. Therefore, according to Eq. (5), the temperature of the radiative cooling surface is expected to increase in the presence of condensed droplets. In fact, the ratio $\alpha_{atm}/\varepsilon_n$ was measured as 0.86 and 0.94 for the dry and droplet-covered samples used in the outdoor experiments.

4.4. Effect of orientation and implications for buildings

While this study has shown that dropwise condensation can affect the spectral properties of the radiative cooling surfaces to impart a broadband emittance, the dew formation depends on several factors including the orientation of the surface [35,36]. Horizontal sky-facing radiative cooling surfaces can cool down to low temperatures and collect more dew thanks to their orientation. On the other hand, vertically-oriented radiative emitters, which are exposed to both the cold sky and the relatively warm earth, may not reach sufficiently low temperatures for dew formation on the surface or condensed droplets may roll-off due to gravity. This was experimentally demonstrated by exposing horizontally and vertically oriented reference samples to the sky on a humid night in Los Angeles. The photograph of Fig. 11 clearly shows that the horizontal section of the radiative cooling surface facing the sky was covered with condensed water droplets. However, negligible condensation was observed on the vertically oriented section of the radiative cooling surface, except for some droplets near the top, even after being exposed to a humid environment for 2 h.

For building envelopes, these results are important. It has been previously shown that for cooling horizontal sky-facing surfaces like roofs, broadband emitters are sufficient and that selective emitters do not offer a significant cooling benefit [8]. In showing that dropwise condensation on horizontal emitters leads to broadband emittance regardless of the emitter, our work shows that the assumed benefits of selective emitters are even smaller when it comes to the largest application of radiative cooling – cooling roofs of buildings [2,16,17,23].

However, recently, it has been shown that for vertical building facades experiencing broadband summertime terrestrial heat gains and wintertime losses, selective emitters can achieve seasonal thermoregulation and energy savings [35]. Since dew formation appears less likely on vertical surfaces even in exceptionally humid environments (Fig. 11), the thermoregulatory benefits of selective emitters will likely persist in both humid and dry operating conditions. In cases when dew may still form on vertical surfaces, hydrophobic coatings which are spectrally selective and unlikely to impact the optical selectivity (Fig. 7(a)) [37,38], can be used to inhibit condensation and aid its runoff. This is the case of the commercially available silicone-based hydrophobic coating Neverwet^{TM}, as illustrated in Figures S8 and S9 in Supplementary Materials.

4.5. Implications for dew harvesting technologies

Since a selective emittance can achieve lower sub-ambient temperature and greater cooling power at sub-ambient temperatures than a broadband emitter [2,23], it is likelier not only to cool below the dew point but also to enable faster dew formation. As the present study demonstrated, dropwise condensation on radiative coolers can limit both benefits. Thus, to maximize dew harvesting using a selective emitter, f_A must be kept to a minimum. This can be achieved by limiting dew formation to the bottom surface of the selective emitter either by using physical barriers to condensation or by making the sky-facing side hydrophobic, as previously discussed [37,38]. Note that this recommendation differs from that made in the literature but for broadband emitting surfaces [19,20,39].

5. Conclusion

This study elucidated a central, and thus far overlooked, challenge facing radiative cooling: the effect of dropwise condensation on the emittance and selectivity of radiative cooling surfaces. Radiative cooling surfaces with and without hydrophobic coatings were covered with acrylic droplets with surface area coverage f_A between 0 and 52% and mean contact angle $\bar{\theta}_c$ between 39° and 62° Droplets were found to significantly increase the spectral normal emittance $\varepsilon_{n,\lambda}$ of the radiative cooling surfaces with increasing droplet surface area coverage f_A and droplet contact angle $\bar{\theta}_c$, particularly outside the atmospheric transparency window, due to absorption by the droplets. Overall, the presence of droplets changed the radiatively selective surface into a broadband emitter. In addition, outdoor nighttime experiments showed that the temperature of the radiative cooling surface increased in the presence of droplets due to the undesirable heat gain from the relatively warm atmosphere. These results establish that dropwise condensation can significantly reduce the infrared selectivity and associated cooling performance under real operating conditions. The conclusions of this study did not contradict the previous findings [19,20]. Instead, it extends the discussion further to selective radiative cooling surfaces. Therefore, our study has large implications for radiative cooling of building envelopes and dew-harvesting technolo-

gies and can inform the feasibility of strategies for using selective emitters for such applications.

Declaration of Competing Interest

The authors declare that they have no known competing financial interests or personal relationships that could have appeared to influence the work reported in this paper.

CRediT authorship contribution statement

Eylul Simsek: Conceptualization, Investigation, Software, Visualization, Writing – original draft, Project administration. **Jyotirmoy Mandal:** Conceptualization, Investigation, Writing – original draft. **Aaswath P. Raman:** Conceptualization, Resources, Writing – review & editing. **Laurent Pilon:** Conceptualization, Resources, Writing – review & editing, Supervision, Project administration.

Data Availability

Data will be made available on request.

Acknowledgement

This material is based upon work supported, in part, by The Scientific and Technological Research Council of Turkey (TÜBİTAK), and the UCLA Hellman Fellows Award. Jyotirmoy Mandal was supported by Schmidt Science Fellows, in partnership with the Rhodes Trust. The authors would like to thank Dr. Keyong Zhu for his MCRT code.

Supplementary materials

Supplementary material associated with this article can be found, in the online version, at doi:10.1016/j.ijheatmasstransfer.2022.123399.

References

[1] F. Trombe, Perspectives sur l'utilisation des rayonnements solaires et terrestres dans certaines régions du monde, Revue Générale Thermique 6 (1967) 1285–1314.
[2] X. Sun, Y. Sun, Z. Zhou, M.A. Alam, P. Bermel, Radiative sky cooling: fundamental physics, materials, structures, and applications, Nanophotonics 6 (5) (2017) 997–1015.
[3] M. Santamouris, J. Feng, Recent progress in daytime radiative cooling: is it the air conditioner of the future? Buildings 8 (12) (2018) 168.
[4] T.L. Bergman, Active daytime radiative cooling using spectrally selective surfaces for air conditioning and refrigeration systems, Sol. Energy 174 (2018) 16–23.
[5] J.N. Munday, Tackling climate change through radiative cooling, Joule 3 (2019) 2057–2060.
[6] X. Lu, P. Xu, H. Wang, T. Yang, J. Hou, Cooling potential and applications prospects of passive radiative cooling in buildings: the current state-of-the-art, Renew. Sustain. Energy Rev. 65 (2016) 1079–1097.
[7] A. Baniassadi, D.J. Sailor, and G.A. Ban-Weiss, "Potential energy and climate benefits of super-cool materials as a rooftop strategy," *Urban Climate*, vol. 29, 100495, 2019.
[8] J. Mandal, Y. Yang, N. Yu, A.P. Raman, Paints as a scalable and effective radiative cooling technology for buildings, Joule 4 (2020) 1350–1356.
[9] N. Agam, P.R. Berliner, Dew formation and water vapor adsorption in semi-arid environments - A review, J. Arid Environ. 65 (4) (2006) 572–590.
[10] D. Beysens, The formation of dew, Atmos. Res. 39 (1995) 215–237.
[11] D. Beysens, The Physics of dew, Breath Figures and Dropwise Condensation, 1st edition, Springer Nature, Switzerland, 2022.
[12] D. Beysens, Dew Water, 1st edition, Rivers Publishers, Gistrup, Denmark, 2018.
[13] T.M.J. Nilsson, W.E. Vargas, G.A. Niklasson, C.G. Granqvist, Condensation of water by radiative cooling, Renew Energy 5 (1994) 310–317.
[14] B. Khalil, J. Adamowski, A. Shabbir, C. Jang, M. Rojas, K. Reilly, B. Ozga-Zielinski, A review: dew water collection from radiative passive collectors to recent developments of active collectors, Sustain. Water Resour. Manag. 2 (2016) 71–86.
[15] E. Rephaeli, A. Raman, S. Fan, Ultrabroadband photonic structures to achieve high-performance daytime radiative cooling, Nano Lett. 13 (4) (2013) 1457–1461.
[16] X. Yin, R. Yang, G. Tan, S. Fan, Terrestrial radiative cooling: using the cold universe as a renewable and sustainable energy source, Science 370 (2020) 786–791.
[17] D. Li, X. Liu, Z. Lin, B. Zhu, Z. Li, J. Li, B. Li, S. Fan, J. Xie, J. Zhu, Scalable and hierarchically designed polymer film as a selective thermal emitter for high-performance all-day radiative cooling, Nat Nanotechnol 16 (2) (2021) 153–158.
[18] G.M. Hale, M.R. Querry, Optical constants of water in the 200-nm to 200-μm wavelength region, Appl. Opt. 12 (3) (1973) 555–563.
[19] J. Trosseille, A. Mongruel, L. Royon, D. Beysens, Effective substrate emissivity during dew water condensation, Int. J. Heat Mass Transf. 183 (2022) 122078.
[20] R. Yang, M. Wang, M. Du, X. Wang, G.H. Tang, Droplet effect on the infrared transmittance of radiative cooler for direct water condensation, Sol. Energy Mater. Sol. Cells 238 (2022) 111615.
[21] X. Huang, J. Mandal, A.P. Raman, Do-it-yourself radiative cooler as a radiative cooling standard and cooling component for device design, J. Photonic. Energy 12 (2021) 012112.
[22] C.S.K. Achoundong, N. Bhuwania, S.K. Burgess, O. Karvan, J.R. Johnson, W.J. Koros, Silane modification of cellulose acetate dense films as materials for acid gas removal, Macromolecules 46 (14) (2013) 5584–5594.
[23] M.M. Hossain, M. Gu, Radiative cooling: principles, progress, and potentials, Adv. Sci. 3 (7) (2016) 1500360.
[24] T.L. Bergman, A.S. Lavine, F.P. Incropera, D.P. Dewitt, Fundamentals of Heat and Mass Transfer, 7th edition, John Wiley & Sons, Hoboken, NJ, 2011.
[25] K. Zhu, L. Pilon, Transmittance of semitransparent windows with absorbing cap-shaped droplets condensed on their backside, J. Quant. Spectrosc. Radiat. Transfer 201 (2017) 53–63.
[26] K. Zhu, S. Li, L. Pilon, Light transfer through windows with external condensation, J. Quant. Spectrosc. Radiat. Transfer 208 (2018) 164–171.
[27] E. Simsek, K. Zhu, G.N. Kashanchi, M.J. Williams, T. Galy, M. Marszewski, S.H. Tolbert, L. Pilon, Light transfer through semi-transparent glass panes supporting pendant droplets, J. Quant. Spectrosc. Radiat. Transfer 261 (2021) 107493.
[28] E. Simsek, M.J. Williams, J. Hoeniges, K. Zhu, L. Pilon, Infrared radiation transfer through semitransparent windows supporting absorbing droplets, Int. J. Heat. Mass Transf. 194 (2022) 123043.
[29] M. Rubin, Optical properties of soda lime silica glasses, Sol. Energy Mater. 12 (1985) 275–288.
[30] A.D. Rakić, R. Rakić, A.B. Djurišˇ, J.M. Elazar, M.L. Majewski, Optical properties of metallic films for vertical-cavity optoelectronic devices, Appl. Opt. 37 (22) (1998) 5271–5283.
[31] X. Zhang, J. Qiu, J. Zhao, X. Li, L. Liu, Complex refractive indices measurements of polymers in infrared bands, J. Quant. Spectrosc. Radiat. Transfer 252 (2020) 107063.
[32] J.W. Rose, L.R. Glicksman, Dropwise condensation - the distribution of drop size, Int. J. Heat Mass Transf. 16 (1973) 411–425.
[33] D. Beysens, C.M. Knobler, Growth of breath figures, Phys. Rev. Lett. 57 (1986) 1433–1436.
[34] B.J. Briscoe, K.P. Galvin, The effect of surface fog on the transmittance of light, Sol. Energy 46 (4) (1991) 191–197.
[35] J. Mandal, S. Mandal, J. Brewer, A. Ramachandran, and A.P. Raman, "Radiative cooling and thermoregulation in the earth's glow," Available: http://arxiv.org/abs/2006.11931 (Accessed: Nov. 18, 2021).
[36] J.C. Howell, T. Yizhaq, N. Drechsler, Y. Zamir, D. Beysens, J.A. Shaw, Generalized nighttime radiative deficits, J. Hydrol. (Amst) 603 (2021) 126971.
[37] B. Figgis, A. Nouviaire, Y. Wubulikasimu, W. Javed, B. Guo, A. Ait-Mokhtar, R. Belarbi, S. Ahzi, Y. Remond, A. Ennaoui, Investigation of factors affecting condensation on soiled PV modules, Sol. Energy 159 (2018) 488–500.
[38] T. Furuta, M. Sakai, T. Isobe, A. Nakajima, Effect of dew condensation on the wettability of rough hydrophobic surfaces coated with two different silanes, Langmuir 26 (16) (2010) 13305–13309.
[39] Z. Zhou, X. Wang, Y. Ma, B. Hu, J. Zhou, Transparent polymer coatings for energy-efficient daytime window cooling, Cell Rep. Phys. Sci. 1 (2020) 100231.